Single particle detection in CMOS compatible photonic crystal nanobeam cavities

Qimin Quan,[1,2] **Daniel L. Floyd,**[1] **Ian B. Burgess,**[1] **Parag B. Deotare,**[1] **Ian W. Frank,**[1] **Sindy K. Y. Tang,**[1] **Rob Ilic,**[3] **and Marko Loncar**[1,*]

[1]*School of Engineering and Applied Science, Harvard University, Cambridge, MA 02138, USA*
[2]*Rowland Institute at Harvard University, Cambridge, MA 02142, USA*
[3]*Cornell NanoScale Science and Technology Facility, Cornell University, Ithaca, NY 14853, USA*
[*]*loncar@seas.harvard.edu*

Abstract: We report the label-free detection of single particles using photonic crystal nanobeam cavities fabricated in silicon-on-insulator platform, and embedded inside microfluidic channels fabricated in poly-dimethylsiloxane (PDMS). Our system operates in the telecommunication wavelength band, thus leveraging the widely available, robust and tunable telecom laser sources. Using this approach, we demonstrated the detection of polystyrene nanoparticles with dimensions down to 12.5nm in radius. Furthermore, binding events of a single streptavidin molecule have been observed.

© 2013 Optical Society of America

OCIS codes: (230.5298) Photonic crystals; (140.4780) Optical resonators; (230.7408) Wavelength filtering devices.

References and links

1. H. K. Hunt and A. M. Armani, "Label-free biological and chemical sensors," Nanoscale **2**, 1544–1559 (2010).
2. X. D. Fan, I. M. White, S. I. Shopova, H. Y. Zhu, J. D. Suter, and Y. Sun, "Sensitive optical biosensors for unlabeled targets: A review," Anal. Chim. Acta **620**, 8–26 (2008).
3. M. Iqbal, M. A. Gleeson, B. Sqaugh, F. Tybor, W. G. Gunn, M. Hochberg, T. Baehr-Jones, R. C. Bailey, and L. C. Gunn, "Label-free bisensor arrays based on silicon ring resonators and high-speed optical scanning instrumentation," IEEE J. Sel. Top. Quantum Electron. **16**, 654–661 (2010).
4. M. Lee and P. M. Fauchet, "Two-dimensional silicon photonic crystal based biosensing platform for protein detection," Opt. Express **15**, 4530–4535 (2007).
5. S. Mandal, J. M. Goddard, and D. Erickson, "A multiplexed optofludic sensor for low mass detection," Lab Chip **9**, 2924–2932 (2009).
6. M. Loncar, A. Scherer, and Y. Qiu, "Phrotonic crystal laser sources for chemical detection," Appl. Phys. Lett. **82**, 4648–4650 (2003).
7. E. Chow, A. Grot, W. L. Mirkarami, M. Sigalas, and G. Girolami, "Ultracompact biochemical sensor built with two-dimensional photonic crystal microcavity," Opt. Lett. **29**, 1093–1095 (2004).
8. C. Y. Chao, W. Fung, and L. J. Guo, "Polymer microring resonators for biochemical sensing applications," IEEE J. Sel. Top. Quantum Electron. **12**, 134–142 (2006).
9. F. Vollmer, S. Arnold, and D. Keng, "Single virus detection from the reactive shift of a whispering gallery mode," Proc. Natl. Acad. Sci. U. S. A. **105**, 20701–20704 (2008).
10. T. Lu, H. Lee, T. Chen, S. Herchak, J.-H. Kim, S. E. Fraser, R. C. Flagan, and K. Vahala, "High sensitivity nanoparticle detection using optical microcavities," Proc. Natl. Acad. Sci. U. S. A. **108**, 5976–5979 (2011).
11. J. Zhu, S. K. Ozdemir, Y.-F. Xiao, L. Li, L. He, D.-R. Chen, and L. Yang, "On-chip single nanoparticle detection and sizing by mode splitting in an ultrahigh-Q microresonator," Nat. Photonics **4**, 46–49 (2009).

12. L. He, S. K. Ozdemir, J. Zhu, W. Kim, and L. Yang, "Detecting single viruses and nanoparticles using whispering gallery microlasers," Nat. Nanotechnol. **6**, 428–432 (2011).
13. V. R. Dantham, S. Holler, C. Barbre, D. Keng, V. Kolchenko, and S. Arnold, "Label-free detection of single protein using a nanoplasmonic-photonic hybrid microcavity," Nano Lett. **13**(7), 3347–3451 (2013).
14. I. Ament, J. Prasad, A. Henkel, S. Schmachtel, and C. Sonnichsen, "Single unlabeled protein detection on individual plasmonic nanoparticles," Nano Lett. **12**, 1092–1095 (2012).
15. P. Zijlstra, P. M. R. Paulo, and M. Orrit, "Optical detection of single non-absorbing molecules using the surface plasmon resonance of a gold nanorod," Nat. Nanotechnol. **7**, 379–382 (2012).
16. P. B. Deotare, M. W. McCutcheon, I. W. Frank, M. Khan, and M. Loncar, "High quality factor photonic crystal nanobeam cavities," Appl. Phys. Lett. **94**, 121106 (2009).
17. Q. Quan, P. B. Deotare, and M. Loncar, "Photonic crystal nanobeam cavity strongly coupled to the feeding waveguide," Appl. Phys. Lett. **96**, 203102 (2010).
18. M. L. Gorodetsky, A. A. Savchenkov, and V. S. Ilchenko, "Ultimate Q of optical microsphere resonators," Opt. Lett. **21**, 453–455 (1996).
19. K. J. Vahala, "Optical microcavities," Nature **424**, 839–846 (2003).
20. J. Voros, "The density and refractive index of adsorbing protein layers," Biophys. J. **87**, 553–561 (2004).
21. F. Vollmer, D. Braun, A. Libchaber, M. Khoshsima, I. Teraoka, and S. Arnold, "Protein detection by optical shift of a resonant microcavity," Appl. Phys. Lett. **60**, 4057–4059 (2002).
22. S. Arnold, M. Khoshsim, I. Teraoka, S. Holler, and F. Vollmer, "Shift of whisper-gallery modes in microspheres by protein adsorption," Opt. Lett. **28**, 272–274 (2003).
23. S. J. McNab, N. Moll, and Y. A. Vlasov, "Ultra-low loss photonic integrated circuit with membrane-type photonic crystal waveguides," Opt. Express **11**, 2927–2939 (2003).
24. D. M. Wieliczka, S. Weng, and M. R. Querry, "Wedge shaped cell for highly absorbant liquids: infrared optical constants of water," Appl. Opt. **28**, 1714–1719 (1989).
25. A. M. Armani and K. J. Vahala, "Heavy water detection using ultra-high-Q microcavities," Opt. Lett. **31**, 1896–1898 (2006).
26. V. R. Dantham, S. Holler, V. Kolchenko, Z. Wan, and S. Arnold, "Taking whispering gallery-mode single virus detection and sizing to the limit," Appl. Phys. Lett. **101**, 043704 (2012).
27. R. W. P. Drever, J. L. Hall, F. V. Kowalski, J. Hough, G. M. Ford, A. J. Munley, and H. Ward, "Laser phase and frequency stablization using an optical resonator," Appl. Phys. B **31**, 97–105 (1983).

1. Introduction

Label-free biomedical and chemical sensors are of enormous importance in healthcare, environmental surveillance and national security [1,2]. Optical cavity sensing methods are based on monitoring shifts of the resonances of high-Q cavities, due to analyte-induced refractive index changes in the near-field of the structure. These changes can be localized perturbations due to the adsorption of analyte onto the cavity surface [3, 5], or a global change in the bulk concentration of the analyte (e.g. differences in glucose concentrations in an aqueous solution) [6–8]. The Q-factor and the mode volume of the cavity are the key parameters that determine the detection limit of these sensors. The ultra-high Q-factors demonstrated in Whispering Gallery Mode (WGM) cavities enabled detection of extremely small resonance shifts induced from single viruses and nanoparticles [9–13]. However, WGM based sensors are difficult to integrate with waveguide and further multiplexing. Recently, plasmonic nanorods have demonstrated detection of single proteins [14, 15]. This is enabled by the ultra-small mode volumes (V) of the surface plasmon mode. The high absorption losses characteristic of most plasmonic systems, however, produces broad resonance lines. In this work, we use photonic crystal nanobeam cavities that combine high Q and small mode volumes. We report the label-free detection of single polystyrene nanoparticles and streptavidin proteins in a CMOS compatible and scalable photonic crystal nanobeam cavity platform. Importantly, our system operates in the telecommunication wavelength band thus leveraging the availability of robust and tunable telecom lasers.

2. Prospect of photonic crystal nanobeam cavity for single molecule sensing

The sensing element that we use in this work is based on a photonic crystal nanobeam cavity [16] (scanning electron microscope image shown in Fig. 1(a), designed using a determinis-
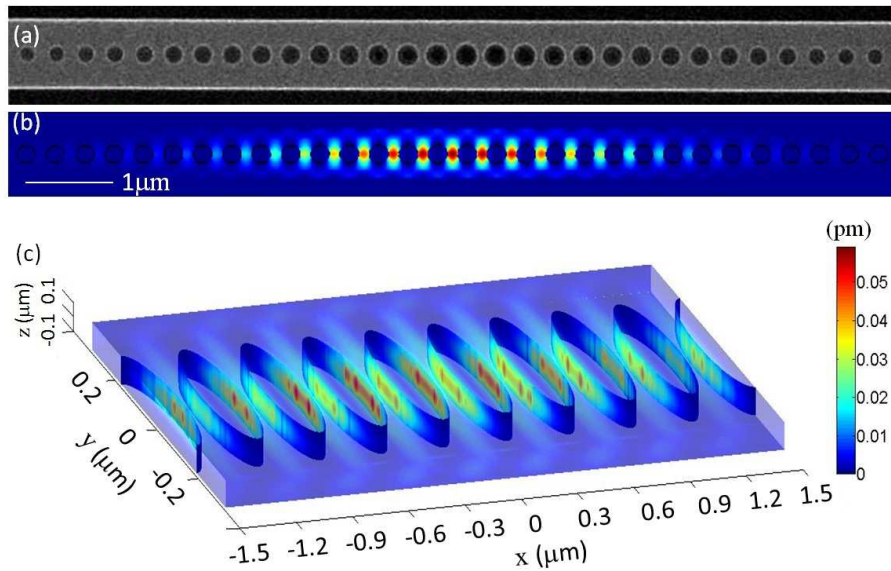
Fig. 1. (a) Scanning electron microscope (SEM) image of a representative silicon nanobeam cavity (top view). (b) Finite-difference time-domain (FDTD) simulation of the energy density distribution in the cavity on resonance, showing an optical mode volume in sub micrometer-cubed scale. (c) The resonance shift induced by single streptavidin molecules, calculated by perturbation theory and mapped to the binding position of the molecule on the nanocavity sensor. The cylinders are the side walls of the holes of nanobeam cavity. The color level indicates the magnitude of the resonance shift.
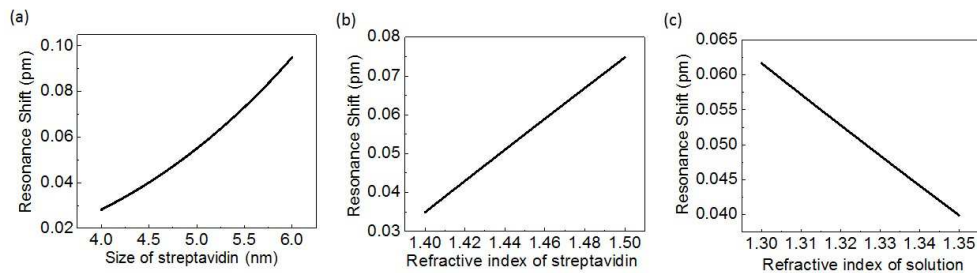

Fig. 2. (a) The maximum resonance shift induced by single solid spherical particle with refractive index 1.45 (model for streptavidin molecule [20]), in a carrying solution with index=1.315. Size refers to the diameter of the spherical particle. (b) The maximum resonance shift for different refractive indices in the spherical particle model (size=5nm, solution index=1.315). (c) The maximum resonance shift for different carrying solution index (streptavidin size=5nm, streptavidin index=1.45).

tic method that we recently developed [17]. Figure 1(b) shows the mode profile of the cavity obtained using finite-difference time-domain (FDTD) modeling. A particle (e.g. virus, protein, or bacterium) brought in the vicinity of the cavity mode perturbs the cavity and causes a slight shift in the cavity resonance. Since the overall perturbation from the particle is proportional to the ratio between particle's size and the cavity's mode volume, photonic crystal nanobeam cavities with mode volumes smaller than the size of a bacterium (typically 2-3 orders of magnitude smaller than those of microsphere resonators [18]), are well suited for biosensing applications [19]. In order to estimate the feasibility of single molecule detection, we choose the streptavidin molecule as the sensing target and calculate the resonance shift induced by a single streptavidin molecule. Since the size of the streptavidin molecule ($\sim$5nm in diameter [20]) is much smaller than the optical wavelength, the variation of the optical field across the molecule can be neglected, and the wavelength shift can be quantitatively calculated with perturbation theory based on the field distribution obtained from FDTD simulation. We model the streptavidin molecule as a solid spherical nanoparticle with permittivity $\varepsilon_p = 1.45^2$ and size (volume) V_{mol} with diameter of 5nm. The cavity resonance shift ($\delta\lambda$) is [21, 22]

$$\frac{\delta\lambda}{\lambda} = \frac{3(\varepsilon_p - \varepsilon_s)}{\varepsilon_p + 2\varepsilon_s} \frac{|\mathbf{E}_{\mathrm{mol}}|^2}{2\int \varepsilon |\mathbf{E}|^2 \mathrm{d}r} V_{\mathrm{mol}} \tag{1}$$

where λ is the resonance wavelength of the nanocavity, ε_s is the permittivity of the surrounding medium, $\mathbf{E}_{\mathrm{mol}}$ is the optical field at the position of the molecule and $\int \varepsilon |\mathbf{E}|^2 \mathrm{d}r$ is the total optical energy stored in the nanocavity. Figure 1(c) plots the predicted resonance shift at different binding sites on the top surface, inside the holes and on the side walls of the cavity. The color level indicates the magnitude of the resonance shift. Approximately a maximum of 0.02pm wavelength shift is expected on the top surface of the cavity, 0.01pm on the side walls and 0.06pm inside the holes of the gratings.

To account for uncertainties in the size and refractive indices of the molecule and carrier fluid, in Fig. 2, we calculate the maximum resonance shift induced by the spherical nanoparticle (model for streptavidin molecule) assuming different particle sizes, particle refractive indices and carrier solution refractive indices. It can be seen that the resonance shift, and therefore the sensitivity of our sensor, is very sensitive to the size of the molecule. Based on the data, we concluded that a maximum resonance shift on the order of 0.04-0.08pm is expected from single streptavidin molecules.

3. Fabrication of on-chip nanobeam cavity sensor

As illustrated in Fig. 3(a), the sensor chip consists of silicon nanobeam cavities, silicon waveguides, polymer spot-size converters, and microfluidic network used for fluid delivery. The silicon nanobeam cavity consists of a tapered array of holes (periodicity 330nm), defined along a 600nm wide ridge waveguide. The device was fabricated on a silicon-on-insulator (SOI) wafer with a 220nm device layer on a 3μm buried oxide. The cavity region was approximately 15μm long. The device was defined by electron-beam lithography using Hydrogen SilsesQuioxane (HSQ) as the resist, followed by reactive ion etching (C$_4$F$_8$/SF$_6$) of silicon. In order to achieve efficient coupling between a commercial tapered optical fiber (Ozoptics inc.) and the silicon waveguide, a polymer fiber-waveguide coupler was employed [17, 23]. The fiber-waveguide coupler consists of a 3μm $\times$ 3μm cross-section polymer (SU-8) waveguide, defined through a second electron-beam lithography step. In the mode conversion section, the width of the silicon waveguide was linearly tapered from 600nm to 50nm over a length of 500μm, in order to adiabatically couple the light from the SU-8 waveguide to silicon waveguide [17]. Current experimental coupling efficiency is 12%, which includes the tapered fiber-polymer waveguide coupling, polymer waveguide - silicon waveguide mode conversion, and propagation losses of
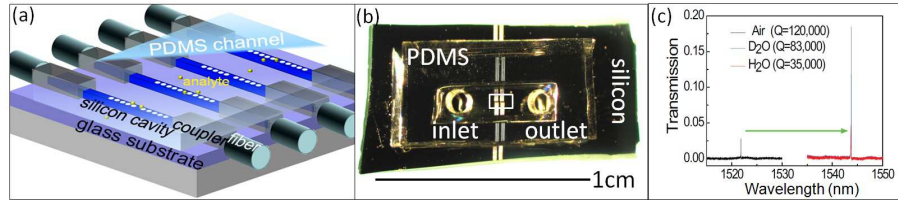
Fig. 3. (a) Schematic (not to scale) of the on-chip optical network sensing platform, which consists of silicon nanocavities, waveguides, polymer fiber-waveguide couplers and optical fibers. PDMS fluidic channel is integrated on top of the chip to deliver analytes to the cavities. (b) Photograph of the device. The two holes are inlet and outlet for introduction of fluids to the PDMS channel. A millimeter-size rectangular channel was permanently sealed on the silicon chip. The bright vertical lines are an array of 14 polymer fiber-waveguide couplers that are connected to 14 silicon nanocavities in the boxed region. (c) Transmission signal from the sensor in air, D_2O and H_2O.

the silicon waveguide. Numerical modeling predicts that this efficiency can be as high as 86% in our design. The discrepancy between theoretical predictions and experimental results are attributed to the scattering at the input facet of the chip (can be improved by polishing the facet) and imperfect alignment between the tapered fiber and the polymer waveguide. Signal transmitted through the cavity was collected with another tapered optical fiber using a similar approach. Our silicon-based optical platform is integrated with a microfluidic channel fabricated in polydimethylsiloxane (PDMS) using replica molding of a SU-8 template. The microfluidic channel has dimensions of $2mm \times 100\mu m \times 50\mu m$ (length×width×height) and is terminated with two millimeter-diameter holes on both ends - inlet and outlet for fluid delivery (Fig. 3(b)).

The transmission signal is obtained by sweeping the tunable laser (Agilent Inc.) source and collecting signal through the cavity with an InGaAs detector (Electro-Optical systems Inc.). The polarization of input and transmitted light was controlled using in-line fiber polarizer in order to improve signal-to-noise ratio by filtering-out the unwanted TM component. The transmission spectrum of a representative cavity operating in air shows prominent cavity resonance with Q of 120,000 (Fig. 3(c)). When air is replaced with D_2O and water, the Q drops to 83,000 and 35,000, respectively. The reduction of Q in the water as compared to D_2O is due to the absorption by water in the telecom wavelength range [24, 25]. Upon immersion in liquid the cavity resonance shifts to longer wavelengths with $\Delta\lambda \approx 22nm$. This is consistent with the theoretically predicted sensitivity of our cavity, which is $\Delta\lambda/\Delta n = 83nm/$RIU (refractive index unit).

4. Nanobeam sensor for single nanoparticle sensing

As a step towards single molecule sensing, we first used the nanobeam sensor to detect single polystyrene nanoparticles. Polystyrene particles with radii of 100nm, 25nm and 12.5nm were dispersed in DI water and injected into the sensor. During the experiment, the cavity resonance was measured every 100 milliseconds for 1 minute. A signal generator was used to scan the wavelength of the laser around the cavity resonance. The transmitted signal was measured using an optical detector, and Lorentzian profile fitting was performed to extract the cavity resonance. The resonance shifts versus time are shown in Fig. 4. The shifts consist of discrete jumps superimposed on the background with a negative slope of $\approx 5pm/min$. We note that this overall slope - also observed in [10, 14], can be attributed to several effects including the oxidization process of the silicon chip, possible physical/chemical deposition processes on the silicon chip from the solution, as well as thermally induced refractive index change of the solution and the silicon chip. In addition, the drift (long-term) and fluctuations (short-term) of the
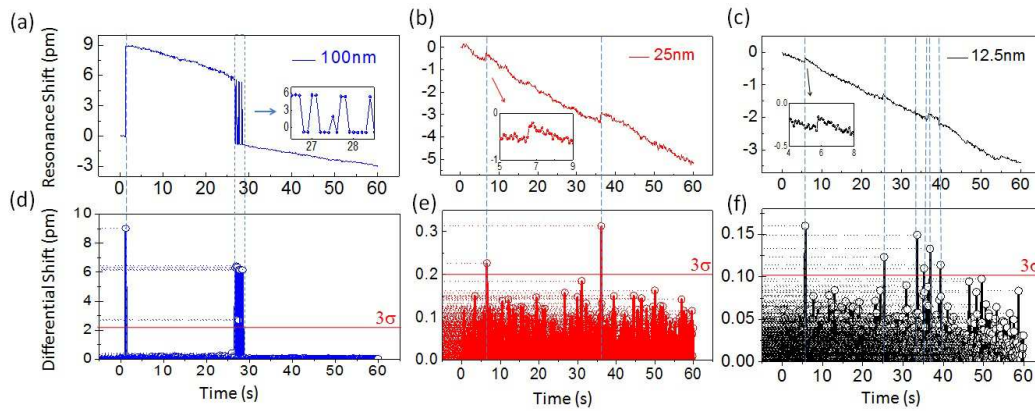
Fig. 4. (a, b & c) Polystyrene particles with radii 100nm, 25nm, 12.5nm were delivered to the sensor through the fluidic channel. The discrete resonance jumps indicate the detection of single nanoparticles. Inset of (a) shows the polystyrene particle diffuses in and out of the sensor. Insets of (b)&(c) zoom in the first resonance jumps in the time trace. (d, e & f) Differential shifts calculated from (a, b & c). The differential shift is defined by subtracting the resonant shifts obtained from two consecutive readouts. Their standard deviation (σ) is analyzed. Single particle events are identified from noise and are marked with dashed lines.
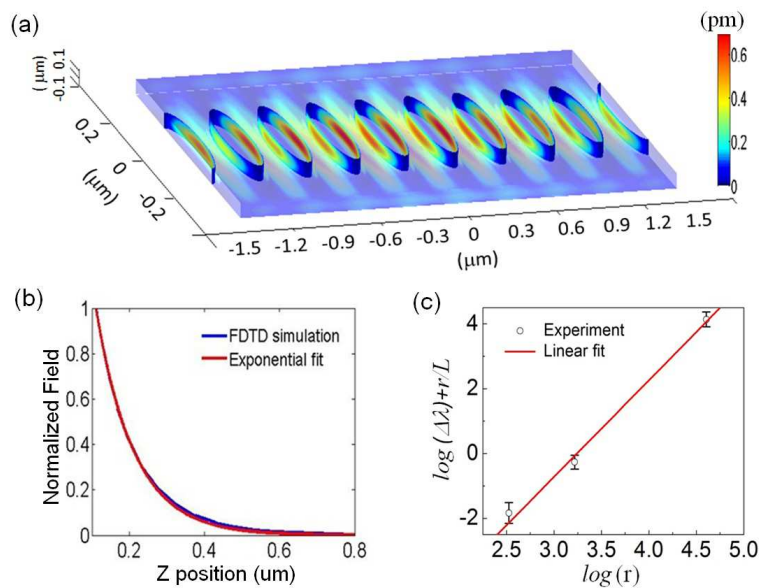

Fig. 5. (a) The resonance shift induced by single 12.5nm-radius polystyrene particles at different binding positions (top surface, side walls, inside holes) of the nanocavity sensor, calculated by perturbation theory. The cylinders are the side walls of the holes of nanobeam cavity. The color level indicates the magnitude of the resonance shift. (b) The evanescent field decay of the optical mode away from the top surface of the nanobeam cavity. (c) The measured resonance shift induced by different size polystyrene particles (symbols) are in good agreement with theoretically predicted scaling rule $\Delta\lambda \propto r^3 e^{-r/L}$ where r is the radius of the particle and L is the characteristic length of the cavity field.

laser output wavelength will also be added on top of the overall slope. In spite of this overall trend, the discrete resonance jumps are obvious for 100nm diameter, polystyrene particles (Fig. 4(a)). During our experiment, the particle solutions were first injected, and measurement was taken after the injection was stopped. The jumps correspond to single polystyrene particles diffusing through the cavity mode region, triggering the resonance shift. Inset of Fig. 4(a) shows the particle moves in and out of the sensor. The jumps can also be seen in the case of 25nm (Fig. 4(b)) and 12.5nm radii nanoparticles (Fig. 4(c)). To determine which jumps correspond to nanoparticles diffusing to the sensor region and which to noise (e.g. temperature drift, laser wavelength fluctuations, etc), we perform 3σ analysis of the detected shifts. We define differential shifts as subtracting the resonant shifts obtained from two consecutive readouts, and then their standard deviation (σ) is analyzed. The differential shifts larger than 3σ are identified as signal (nanoparticle crossing the sensor), and everything else as noise. The data are summarized in Figs. 4(d), 4(e), and 4(f): single-particle detection events can be observed even for 12.5nm-radius nanoparticles, which are the smallest available polystyrene nanoparticles.

We performed the perturbation calculation (same as Fig. 1(c)) for the 12.5nm-radius polystyrene nanoparticle, neglecting the field variation across the nanoparticle. Note that in this case, the field distribution is obtained from FDTD simulation. To account for the nanoparticle size, the field intensities that are in the plane 12.5nm above the surface of the nanobeam are utilized. Approximately a maximum of 0.2pm wavelength shift is expected on the top surface of the cavity, 0.1pm on the side walls and 0.7pm inside the holes of the gratings (Fig. 5(a)). Experimentally we observed about 0.17pm shift for 12.5nm-radius polystyrene particle. This indicates that polystyrene particles are most likely adsorbed on the top surface.

Since polystyrene particles range from tens to hundred nanometers, the field decay due to the finite size of the nanoparticles can be accounted with the following scaling rule $\Delta\lambda \propto r^3 e^{-r/L}$ [22] where $\Delta\lambda$ is the resonance shift, r is the radius of the particle, L is the evanescent decay-length of the cavity field on the top surface. The value of $L = 51$nm was obtained from FDTD simulation by fitting the evanescent field outside the cavity to an exponentially decaying profile (Fig. 5(b)). The average values of experimentally measured resonance shifts obtained from three different particle sizes are shown in Fig. 5(c), in log-log scale, along with the theoretical fit of the form $\log(\Delta\lambda) + r/L = \text{slope} \cdot \log(r) + \text{constant}$. A fit gives a slope-value of 2.98 ± 0.17, that is $r^{2.98}$ dependence of the resonance shift on the nanoparticle radius. This is in excellent agreement with theoretically predicted r^3 dependence. This further confirms that jumps in the cavity resonance are due to individual polystyrene nanoparticles.

5. Nanobeam cavity for single molecule sensing

Next, we use the nanocavity sensor to detect streptavidin molecules in phosphate buffered saline (PBS) solution. In this experiment, sensors were functionalized with biotin for efficient capture. To achieve this, the chip was first cleaned by oxygen plasma and immersed in 2% 3-aminopropyltrimethoxysilane in ethanol for 10 minutes, rinsed thoroughly and heated at 80°C for 2 hours. The chip was then functionlized with an amine reactive biotin derivative, 6-((biotinoyl)amino)hexanoic acid succinimidyl ester (Biotin X SE, Invitrogen) dissolved in a mixture of dimethyl sulfoxide (DMSO) and 0.1M sodium bicarbonate. The real-time responses of our cavity to PBS and 2pM streptavidin are shown in Fig. 6. Like the polystyrene nanoparticles, the existence of the discrete jumps indicates the observation of individual molecules entering the cavity region. These jumps are identified by analyzing the differential shifts the same way as in the nanoparticle case, and are marked by dashed lines in Fig. 6. In the case of blank PBS (Fig. 6(a)), all differential shifts but one fall below the 3σ line (Fig. 6(b)). At 2pM concentration (Fig. 6(c)), multiple differential shifts are greater than the 3σ-level (Fig. 6(d)), and thus attributed to the observation of streptavidin events. We note that the 3σ values calculated from
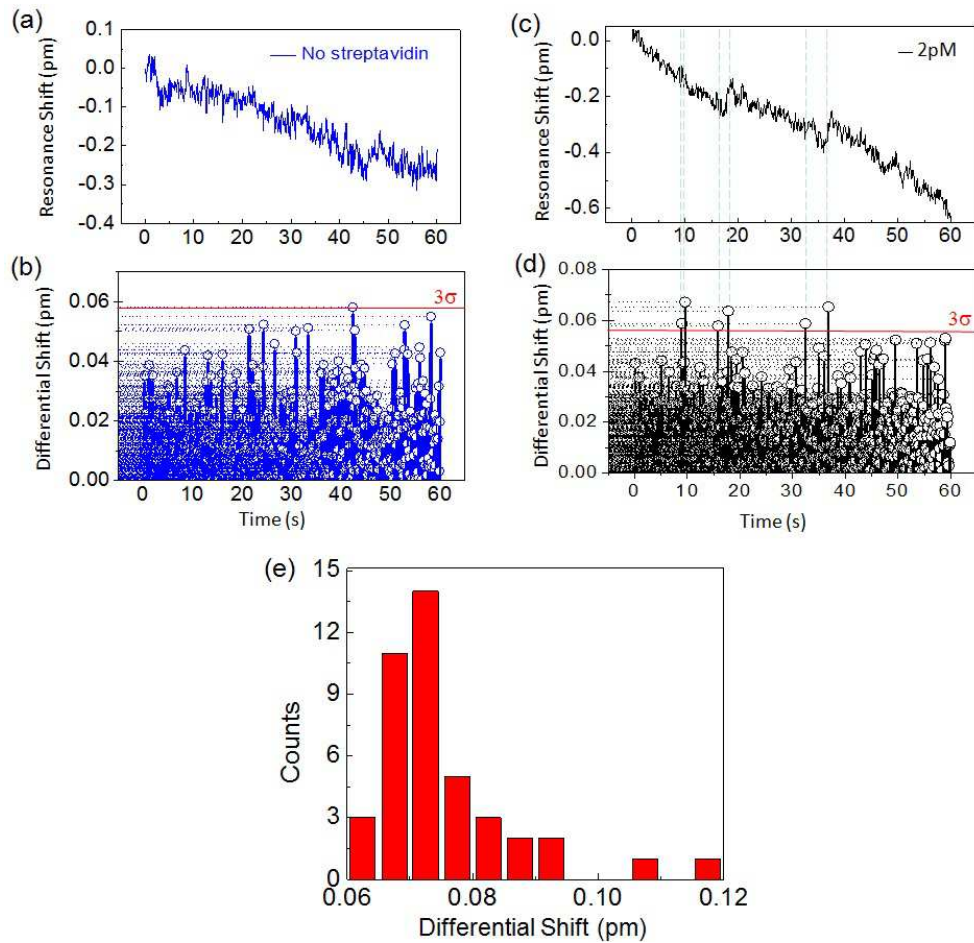
Fig. 6. (a & c) Real-time response of blank PBS and 2pM streptavidin PBS. (b & d) Differential shifts calculated from (a) & (c). Single particle events are identified from noise and are marked with dashed lines. (e) Histogram of the resonance jump events extracted from repeated experiments.

the bare PBS solution and 2pM streptavidin solution have negligible differences, due to small effect of streptavidin to the solution. A histogram of experimental resonance jumps (using the above mentioned 3σ method), accumulated from several experiments is shown in Fig. 6(e). It cuts off at 0.06pm, which is the detection limit of current nanocavity sensor. Furthermore, it can be seen that the most common resonant shift observed in our experiment is 0.07pm, which is within the 0.04-0.08pm range, predicted using theoretical analysis (Fig. 2). The discrepancy between experimental data and theoretical predictions can be attributed to: (i) uncertainties in the size and refractive index of streptavidin, (ii) additional mechanisms that induce additional resonance shift induced by streptavidin (iii) events of pairs or clusters of streptavidins binding on to the nanosensor.

The minimum wavelength shift that can be reliably measured in our system depends on the accuracy in determining the absolute value of the cavity resonance, which in turn depends on the signal-to-noise ration (SNR) of the transmission spectrum measurement. Previous work [14, 26] with similar noise level to ours and SNR$\sim$20dB has demonstrated the ability to extract the cavity resonance (using Lorentzian fitting) with the accuracy of 1/1000th of the resonance linewidth. In our case, this would correspond to an accuracy of $\sim$0.04pm (cavity Q=35,000). Unfortunately, our current measurements fall slightly short off this value, which is attributed to the wavelength fluctuations of the tunable laser source used in our measurements. Using a high resolution wavemeter (Toptica Inc.), we measured the wavelength fluctuation of the laser to be $\sim$70fm, which is on par with the signal from single streptavidin. We found that laser fluctuations are highly dependent on the acoustic noise in the laboratory. For example, we could improve the wavelength stability simply by placing the laser on the sturdy heavy duty table and surrounding it with acoustic foam. This cuts of the wavelength fluctuation in half. Further improvements in the laser stability are still needed in order to reduce the rate of false positive events, and to reach the true potential of our sensor. This will be accomplished by further reducing the acoustic noise in the setup, choosing more stable laser sources or actively stabilizing the laser source with Pound-Drever-Hall technique [27]. Furthermore, an improved cavity design with greater resonance shift to single molecules will also improve the detection of single molecules.

6. Conclusion

In conclusion, we have demonstrated label-free nanoparticle detection and protein detection with single particle sensitivity and single molecule visibility. While single protein detection has been observed recently with hybrid plasmonic-photonic systems [13] and plasmonic nanorods [14, 15], our SOI based platform offers unique advantages, including inexpensive and scalable fabrication using established CMOS processes. The top down fabrication approach also enables highly multiplexed detection with multiple sensors and further integration with electronics and instrumentation. Additionally, the ultra-small mode volume of our cavity makes single molecule detection possible in water, which has proven to be a major limitation of other silicon-based optical cavity sensors. Our device will enable study of biomolecular interactions where fluorescent labeling is not feasible or where sensitivity of current available label-free sensor platforms is inadequate.